

CALCULATION AND EVALUATION OF BRG CORRECTION FACTORS FOR RAILROAD  
VALLEY PLAYA

by

Josephine M. Maxwell

---

Copyright © Josephine M. Maxwell 2022

A Thesis Submitted to the Faculty of the

WYANT COLLEGE OF OPTICAL SCIENCES

In Partial Fulfillment of the Requirements

For the Degree of

MASTER OF SCIENCE

In the Graduate College

THE UNIVERSITY OF ARIZONA

2022

THE UNIVERSITY OF ARIZONA  
GRADUATE COLLEGE

As members of the Master's Committee, we certify that we have read the thesis prepared by Josephine May Maxwell, titled *Calculation and Evaluation of BRF Correction Factors for Railroad Valley Playa* and recommend that it be accepted as fulfilling the dissertation requirement for the Master's Degree.

J S Czaplak Myers  
Professor Jeffrey S. Czaplak-Myers

Date: 26 APR 2022

R. John Koshel  
Professor R. John Koshel

Date: 26 APRIL 2022

Ronald G. Driggers  
Professor Ronald G. Driggers

Date: 26 APR 2022

Final approval and acceptance of this thesis is contingent upon the candidate's submission of the final copies of the thesis to the Graduate College.

I hereby certify that I have read this thesis prepared under my direction and recommend that it be accepted as fulfilling the Master's requirement.

J S Czaplak Myers  
Professor Jeffrey S. Czaplak-Myers  
Master's Thesis Committee Chair  
Wyant College of Optical Sciences

Date: 26 APR 2022

## Table of Contents

List of Figures .....	4
Abstract .....	6
Introduction.....	7
Section 1 – BRF and Field Measurements.....	10
1.1 Defining Terms .....	10
1.2 Measuring HCRF in the Field.....	11
1.2.1 Wide FOV Camera .....	12
1.2.2 PARABOLA .....	13
1.2.3 ULGS-II .....	14
Section 2 – Data Processing.....	15
2.1 Band Averaging .....	16
2.2 Shadow Removal and Azimuth Conversion.....	18
2.3 Correction Factor Calculation.....	19
2.4 Sentinel-2A and B Data .....	20
2.5 Averaging Datasets .....	22
Section 3 – Results.....	24
3.1 Application of Correction Factors .....	24
3.2 Sources of Uncertainty.....	28
Section 4 – Conclusion .....	29
References.....	30

## List of Figures

Figure 1: Landsat 8 OLI image of Railroad Valley Nevada, USA. The purple square indicates the RadCaTS location and size.....	8
Figure 2: (Left) Diagram showing bidirectional reflectance measurement. (Right) Diagram showing hemispherical-conical reflectance measurement. Note strong directional component of the hemispherical illumination due to the sun.....	11
Figure 3: Basic diagram of HCRF measurement using wide FOV camera showing fisheye lens, detector array, and mounting mast.....	12
Figure 4: Simple diagram of the PARABOLA III based on pictures and descriptions in [17] and [18].....	13
Figure 5: Simplified diagram of ULGS-II based on images and descriptions in [20].....	14
Figure 6: Plot of solar altitude vs. time of collection for each of the 13 datasets collected by the ULGS-II at Railroad Valley on May 3 <sup>rd</sup> , 2018.....	15
Figure 7: Nadir reflectances measured during each of the 13 measurement sets, averaged over all wavelengths.....	16
Figure 8: Average spectral reflectance measured at nadir by ULGS-II on May 3 <sup>rd</sup> , 2018 and relative spectral responses of MSI bands 1-9 on Sentinel-2A and 2B.....	17
Figure 9: HCRF data collected by ULGS-II at approximately 18:00 UTC on May 3 <sup>rd</sup> , 2018 in Railroad Valley Playa. Results shown have been band-averaged to correspond to Sentinel 2A MSI band 5. The top plot features a shadow at 260° instrument-referenced azimuth angle indicating the solar azimuthal position. The data in the bottom plot have been shifted such that the azimuth angle refers to the angle to the solar principal plane and the shadow has been removed.....	19
Figure 10: Correction factors determined using the HCRF data that are shown in Figure 9.....	20
Figure 11: BOA surface reflectance values measured by GVRs and Sentinel-2 during 2021. Values have been averaged over all MSI bands of interest.....	21

Figure 12: Relative azimuth angle vs. time of year for each of the Sentinel 2 view configurations. A relative azimuth of $0^\circ$ corresponds to the backscatter direction.....	21
Figure 13: Solar zenith angles during 2021 Sentinel-2 overpasses of Railroad Valley Playa. Red indicates the range of solar zenith angles sampled by the ULGS-II on May 3 <sup>rd</sup> , 2018....	22
Figure 14: Correction factors from Figure 10 with the range of Sentinel 2 overpass view angles indicated. Sampled HCRF angles for the $11^\circ$ overpass configuration are indicated in red and angles for the $6^\circ$ configuration are shown in yellow.....	23
Figure 15: Standard deviation of MSI band 5 correction factors with respect to dataset. Values corresponding to $11^\circ$ and $6^\circ$ overpass configurations are again indicated in red and yellow, respectively.....	23
Figure 16: Correction factors calculated from HCRF data for view zenith $20^\circ$ , relative view azimuth $20^\circ$ , and MSI band 5 plotted against the solar zenith angle during the HCRF measurement.....	24
Figure 17: Percent error between uncorrected (left) and corrected (right) GVR-measured reflectances and MSI-derived BOA surface reflectances.....	25
Figure 18: Percent error for $11^\circ$ VZA overpasses before and after correction.....	26
Figure 19: Comparisons using uncorrected and corrected GVR reflectances for $6^\circ$ overpass.....	26
Figure 20: Average surface reflectance vs. time for 2021 Sentinel 2A and B overpasses.....	27
Figure 21: Percent error plots with low reflectance dates removed.....	28

## Abstract

Applications ranging from military reconnaissance to climate studies depend on the data collected by spaceborne remote sensors. Vicarious calibration is one method by which these sensors are validated. At the Radiometric Calibration Test Site (RadCaTS) in Railroad Valley Playa, Nevada, several autonomous ground viewing radiometers (GVRs) measure the surface reflectance at a nadir view. These data can then be used to calibrate sensors that view the playa from space. The process works well for sensors that view the playa at nadir, but uncertainty increases when the sensors view the playa at large zenith angles due to the non-Lambertian nature of the playa surface. However, if the bidirectional reflectance factor (BRF) of the surface is determined through models or measurement, it is possible to calculate a correction factor that converts a nadir reflectance value to the expected reflectance at an arbitrary view angle. Using preliminary surface measurements taken by the University of Lethbridge Goniometer System II (ULGS-II), correction factors were calculated which improved the agreement between the bottom of atmosphere (BOA) reflectances determined by RadCaTS and those measured by the Sentinel-2A and -2B Multispectral Instrument (MSI) for a view zenith angle (VZA) of  $11^\circ$ .

## Introduction

The data retrieved from satellite sensors enables a plethora of essential science goals. From spotting tropical storms, to monitoring cropland use, to measuring the impact of wildfires, the modern world would be a very different place without the data provided by spaceborne sensors. However, taking measurements of Earth from space is not without challenges. Once a satellite is launched the physical sensors onboard are out of reach of the engineers who built them. Even with extremely careful prelaunch calibration, instrument response can drift over time as components degrade in the harsh environment of space. An onboard calibration system can help, but these systems can also degrade over time. These onboard calibration systems are also typically included as part of flagship systems, and many smaller cubesats do not have onboard calibration systems. Thus, methods have been devised to remotely calibrate these remote instruments, including cross-calibration with other sensors, measurements of the moon, and ground-based measurements [1-3].

Once such ground-based method is the reflectance-based approach to vicarious radiometric calibration [4-5]. In this method, in situ measurements of surface reflectance are collected at a vicarious calibration site at the same time as the satellite sensor of interest passes over the site. Atmospheric and solar irradiance measurements are also collected at the time of overpass [6]. These data are used to calculate the expected top-of-atmosphere (TOA) radiance (or reflectance) at the satellite sensor. The expected radiance is compared to the sensor measurements of the site to obtain calibration coefficients.

It should be immediately apparent that the ground instruments are not measuring the same surface area as the space sensor. Ground measurements must be collected within a few minutes of the overpass to minimize error due to illumination or atmospheric changes, and satellite sensor pixels often have footprints of 10 m to 30 m on the ground. This method requires a highly uniform site that is large enough to fill the field of view of at least one of the pixels of the spaceborne sensor, such that measuring a relatively small percentage of that pixel footprint area will give a satisfactory average reflectance for the full region.

One such site is the Radiometric Calibration Test Site (RadCaTS) located in Railroad Valley Playa, Nevada, USA. A Landsat 8 Operational Land Imager (OLI) image of Railroad Valley is shown in Figure 1.

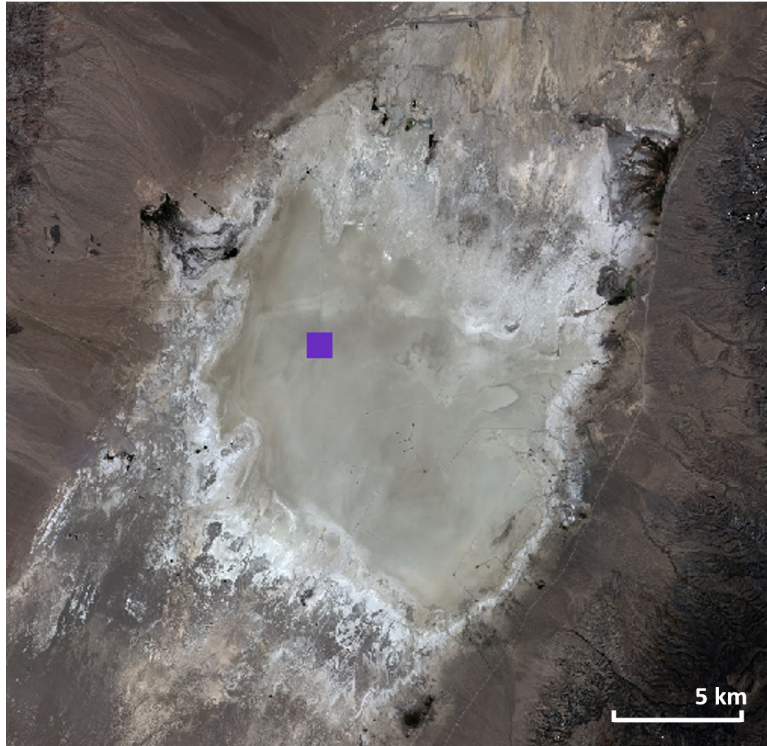


*Figure 1: Landsat 8 OLI image of Railroad Valley Nevada, USA. The purple square indicates the RadCaTS location and size.*

Railroad Valley Playa is a suitable site for vicarious calibration because it provides a relatively high, uniform reflectance over an area that is large enough to accommodate sensors with pixel footprints of greater than  $1 \text{ km}^2$  [5]. Additionally, the playa is located in a high, dry desert environment, which means rainfall is infrequent and aerosol loading of the atmosphere tends to be low. The playa is largely free of vegetation, which means seasonal variability in reflectance is low. Finally, the playa reflectance is approximately spectrally flat between 600 nm and 2000 nm.

RadCaTS is located at  $38.497^\circ \text{ N}$  and  $115.690^\circ \text{ W}$  in a  $1 \text{ km} \times 1 \text{ km}$  region chosen for its suitable representation of the reflection characteristics of the playa as a whole [7]. The Remote Sensing Group (RSG) of the Wyant College of Optical Sciences at the University of Arizona has developed and currently maintains a suite of autonomous instruments within the test site, including seven custom ground viewing radiometers (GVRs) [8-9], a Cimel solar radiometer [10], and other instruments that collect ancillary data such as temperature, pressure, windspeed and direction, and precipitation [6]. The nadir-viewing GVRs collect multispectral data of the surface from 09:00 to 15:00 local standard time (UTC - 8 h) every two minutes during clear sky conditions. The

multispectral data are then fitted to a library of hyperspectral bottom-of-atmosphere (BOA) reflectance measurements of the playa that were collected over the past 25 years by RSG personnel using a portable spectroradiometer. The BOA and TOA reflectances are then calculated using the corresponding measurements from the solar radiometer and other supporting instruments as inputs into a radiative transfer code. RSG currently uses the MODerate resolution radiometric TRANSfer (MODTRAN) code, which was developed by the Air Force Research Laboratory [11]. The RadCaTS end products are the BOA and TOA reflectance at Railroad Valley in 30 minute and 10 nm intervals from 400 nm to 2500 nm, along with the corresponding local atmospheric data. These data are uploaded to the Radiometric Calibration Network (RadCalNet, [www.radcalnet.org](http://www.radcalnet.org)), where they are freely available for scientists and engineers who wish to perform their own vicarious calibration studies.

The RadCaTS GVRs are currently in their second generation, with a third generation under development [12]. The goal is always to reduce uncertainty in the calibration measurements, and the seven GVRs currently in use have been shown to represent the surface reflectance of the overall 1 km<sup>2</sup> region of interest (ROI) at RadCaTS to within  $\pm 0.5\%$  [7]. This is due in large part to the high uniformity of the playa. However, the playa is missing one of the characteristics of an ideal vicarious calibration test site – it is not a perfect Lambertian surface. The reflectance properties of the playa vary with angle. Small rocks, dirt clods, efflorescent salts that appear after rainfall, and cracks in the playa surface cast shadows, which reduce the average surface reflectance. Those shadows appear smaller as the view angle of a sensor approaches the angle at which the sun is illuminating the playa. This results in a hotspot in the backscatter direction as well as a lower BRDF in the forward scatter direction.

When the satellite sensor views the playa with a near-nadir VZA, this phenomenon has minimal impact on the measurements. However, some satellite sensors view the playa at nonzero zenith angles, and angular reflectance effects can introduce significant disagreement between the measured and predicted TOA reflectance values [13].

In theory, if the angular reflectance properties are known for the site at the time of the overpass, a correction factor can be calculated that will allow measurements from nadir-viewing GVRs to be used in the calibration of an off-nadir-viewing satellite sensor. This thesis presents the calculation and application of such correction factors to GVR reflectance measurements corresponding to

Sentinel-2 overpasses. In Section 1, surface reflectance terms are defined and their field measurement is discussed. Section 2 describes the processing of the data used to calculate the correction factors. In Section 3, the results of applying the correction factors to Sentinel-2 overpass GVR measurements is analyzed and sources of uncertainty are discussed. Finally, this thesis concludes in Section 4.

## Section 1 – BRF and Field Measurements

### 1.1 Defining Terms

The angular reflectance properties of a surface are described by that surface's bidirectional reflectance distribution function (BRDF). The BRDF is the ratio of the differential radiance reflected from a surface to the differential irradiance incident on that surface, and therefore has units of inverse steradians [ $\text{sr}^{-1}$ ]. It is a directional quantity, and therefore is a function of four angles – two which describe the orientation of the illuminating ray, and two which describe the reflected ray that is being viewed.

$$BRDF(\theta_i, \phi_i; \theta_r, \phi_r) = \frac{dL_r(\theta_r, \phi_r)}{dE_i(\theta_i, \phi_i)} [\text{sr}^{-1}]$$

For a Lambertian surface, the BRDF is constant with angle.

Frequently, the bidirectional reflectance factor (BRF) is used instead of the BRDF. The BRF is the ratio of differential flux reflected from a surface to the differential flux that would be reflected from an ideal Lambertian reflector. Like the BRDF, BRF is a directional quantity and depends on the angles of the illuminating and reflected rays. Unlike the BRDF, the BRF is unitless.

$$BRF(\theta_i, \phi_i; \theta_r, \phi_r) = \frac{d\Phi_r(\theta_i, \phi_i; \theta_r, \phi_r)}{d\Phi_{r,ideal}(\theta_i, \phi_i; \theta_r, \phi_r)}$$

Both of these quantities are ratios of differential quantities in directional illumination and viewing geometries. As such, neither can be directly measured for a given surface. No source is small enough as to provide directional illumination on a surface, and the collection aperture of the measuring instrument must be finite in area to collect any light. In practice, most field measurements of surface angular reflectance properties measure the hemispherical-conical reflection factor (HCRF). This is because both the sun and sky illuminate the target, and the

viewing geometry is conical due to the finite aperture size of the radiometer being used. The differences between bidirectional and hemispherical-conical measurements are illustrated in Figure 2. A further discussion of these and related reflectance terms can be found in Schaepman-Strub et al. [14].

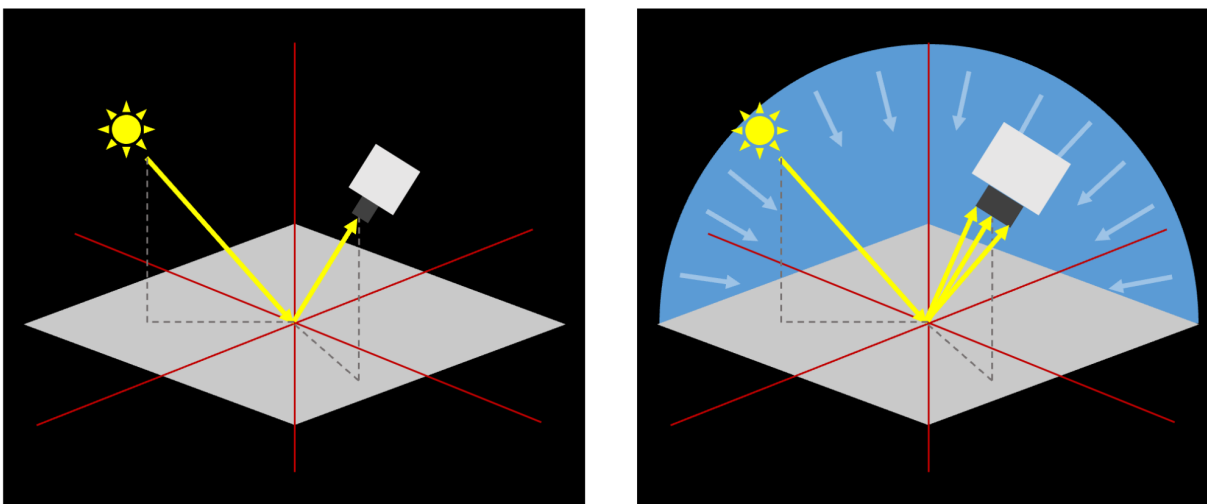


*Figure 2: (Left) Diagram showing bidirectional reflectance measurement. (Right) Diagram showing hemispherical-conical reflectance measurement. Note strong directional component of the hemispherical illumination due to the sun.*

At Railroad Valley, the low aerosol loading of the atmosphere means the sky contribution to illumination of the playa surface is low on clear days [15]. The collection apertures of the radiometers used to measure the surface reflectance are also designed to be small relative to their mounting height. Since the angular size of the sun is small, HCRF measurements can be used to approximate the BRF of the playa.

## 1.2 Measuring HCRF in the Field

Unfortunately, measuring the HCRF of a natural surface is not a trivial task. The sun's angular position changes throughout the day, and the reflected flux must be measured from multiple view angles for each chosen sun position. There are multiple methods by which HCRF is measured in the field. This work focuses on three methods that have been used at Railroad Valley.

### 1.2.1 Wide FOV Camera

In the 1990's, the Remote Sensing Group collected HCRF measurements of the playa using a custom-built wide field of view camera composed of a fisheye lens and a detector array [13]. A simplified diagram of the camera system is shown in Figure 3.

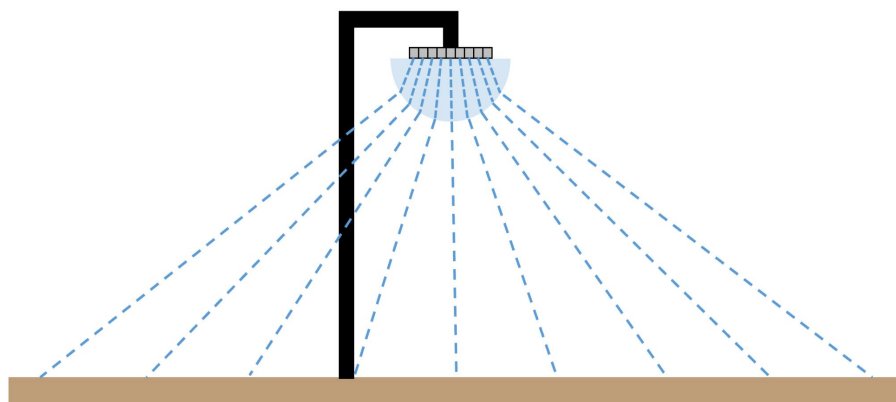


*Figure 3: Basic diagram of HCRF measurement using wide FOV camera showing fisheye lens, detector array, and mounting mast.*

The main benefit of using a wide FOV camera is that measurements can be taken very quickly, as each pixel of the detector array can simultaneously measure the flux for a different set of view angles. However, it also has some disadvantages. Calibrating the detector array requires finding gain and offset values for every pixel in the array, and the lens transmission function must be measured as a function of angle [16]. Both of these lead to a very labor-intensive calibration process. There are also strong Fresnel effects at both the lens and detector array surface which lead to significant polarization aberrations at large zenith angles [16]. The camera also required a cooling system composed of a radiator, antifreeze, and an ice bath to keep the detector cold, which made the instrument difficult to set up in the field.

The Remote Sensing Group collected surface measurements using the wide FOV camera to illustrate the errors that could be encountered when using uncorrected nadir reflectances in the vicarious calibration of off-nadir viewing sensors. It was found that for a  $45^\circ$  view zenith angle, the surface reflectance was up to 6 % greater than what was measured at nadir, with the greatest difference occurring in the backscatter direction [13].

### 1.2.2 PARABOLA

In the summer of 2018, several research groups met at Railroad Valley Playa to collect surface measurements using various instruments and methods. One of those instruments was the NASA JPL Portable Apparatus for Rapid Acquisition of Bidirectional Observation of Land and Atmosphere III (PARABOLA III) [17]. The PARABOLA III is composed of a custom head and a mounting mast. Multiple radiometers on the head can be rotated up and down, while the head itself can be rotated around the axis of the mounting mast. This allows the instrument to collect approximately bidirectional measurements of both the ground and sky without being repositioned. A simplified diagram of the PARABOLA III is shown in Figure 4.

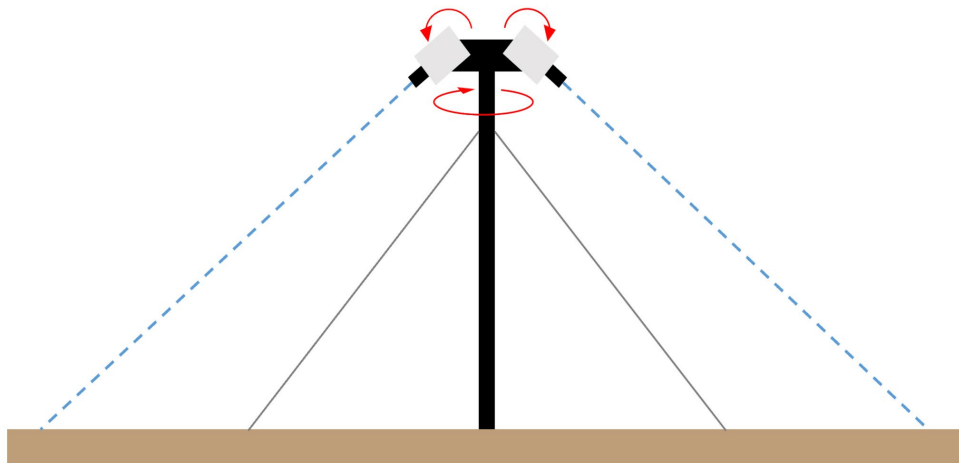


*Figure 4: Simple diagram of the PARABOLA III based on pictures and descriptions in [17] and [18].*

The radiometers must pivot into position and measure each desired view angle individually, so data collection is slower than with the camera. However, this instrument does not suffer from the same Fresnel effects and polarization aberrations since the light being measured enters the radiometers near normal incidence.

The PARABOLA III has collected multiple datasets between 2011 and 2019 from four sites located within Railroad Valley playa [19]. These data have been fit to a modified Rahman-Pinty-Verstraete function, which yields three coefficients that can be used to calculate the expected reflectance for arbitrary view and illumination geometries. Bruegge et al. looked specifically at two view angles relevant to the Orbiting Carbon Observatory (OCO) and Greenhouse Gases Observing Satellite (GOSAT). These platforms view the playa from the west at a zenith of  $30^\circ$  and

from the east at a zenith of  $20^\circ$ . The former corresponds roughly to the backscatter direction and the latter to the forward scatter direction for the overpass times of interest. Bruegge et al. found that the  $30^\circ$  W reflectance tended to be about 8 % higher than the value at nadir, while the  $20^\circ$  E reflectances on average were 8.6 % lower than at nadir.

The PARABOLA results were also found to be generally consistent between sites and measurement dates, suggesting that the surface BRF is spatially and temporally invariant so long as there has not been any recent rainfall [19].

### 1.2.3 ULGS-II

Another instrument that was employed at the 2018 fieldtrip was the University of Lethbridge Goniometer System II (ULGS-II) [20]. The ULGS-II is designed to position the foreoptic of a spectroradiometer such that it points at a specific area on the surface of interest at any desired view angle. The view zenith is selected by changing the position of the foreoptic along a quarter-arc rail. That quarter-arc rail can be rotated about a central mast, which allows the view azimuth to be selected as well. A simple diagram of this instrument is shown in Figure 5.

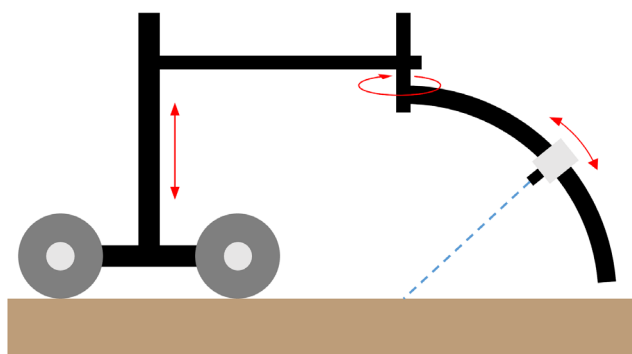


*Figure 5: Simplified diagram of ULGS-II based on images and descriptions in [20].*

The instrument actually employs two spectroradiometers. One is attached to the goniometer arm, as pictured in Figure 5, and measures the flux reflected from the sample surface. The other tracks downwelling radiation using a cosine-corrected Spectralon head. The ratio of the outputs of these two devices yields the HCRF of the surface at each angle measured by the goniometer. The two spectroradiometers are cross-calibrated before each measurement set using a Spectralon reference panel.

Unlike the PARABOLA and wide FOV camera systems that require large, uniform areas to operate, this instrument can measure the HCRF of a relatively small area. It also collects hyperspectral data in the VNIR region of the spectrum (350 nm to 1000 nm), while the other two instruments only collect multispectral measurements. However, this method is the slowest of those described at collecting a full set of measurements, with most of the time going towards repositioning the circular arc and radiometer foreoptic [20].

## Section 2 – Data Processing

The ULGS-II collected multiple datasets on multiple days throughout the 2018 fieldtrip, but the best sky conditions occurred on May 3<sup>rd</sup> 2018. On this date, 13 measurement sets were collected between 15:59 and 22:38 UTC (8:59 am and 3:38 pm local time). The solar altitudes sampled by these measurement sets are shown in Figure 6. In each of these sets, the surface reflectance was measured at zenith angles of 10° to 60° in 10° increments, and azimuthal angles of 0° to 350° in 10° increments. The reflectance at nadir was also sampled 8 times throughout each measurement set. The spectroradiometer sampled these data at wavelengths from 400 nm to 1000 nm in 10 nm increments.

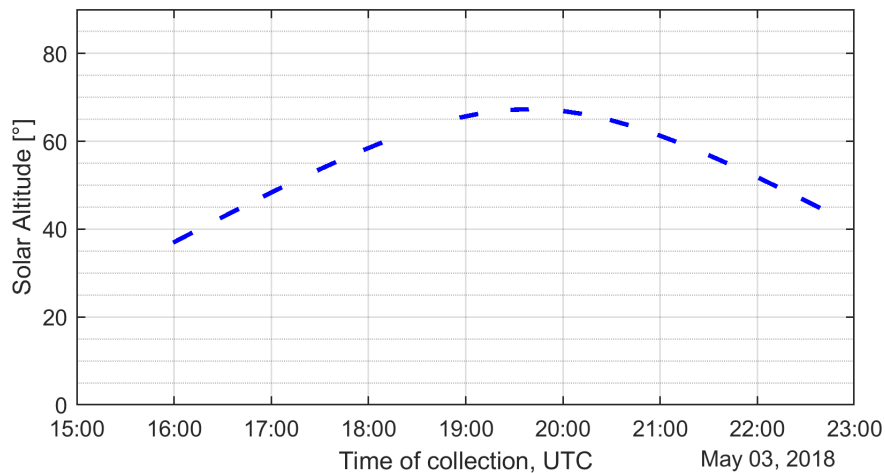


*Figure 6: Plot of solar altitude vs. time of collection for each of the 13 datasets collected by the ULGS-II at Railroad Valley on May 3<sup>rd</sup>, 2018.*

As described in Section 1.2.3, the ULGS-II measured surface reflectance and down welling irradiance simultaneously. The data are then recorded as the ratio of these two measurements, which yields an HCRF for each angle and wavelength measured. These data were read into

MATLAB and formatted into a four-dimensional matrix with size  $6 \times 36 \times 61 \times 13$ , corresponding to the view zenith, view azimuth, wavelength, and measurement set of each HCRF.

During preliminary analysis of the data, it was found that all of the reflectance values measured during the first set, and a portion of the values from the second set, were significantly higher than expected. This is illustrated in Figure 7, where the nadir values are shown for each measurement set, averaged over all wavelengths.

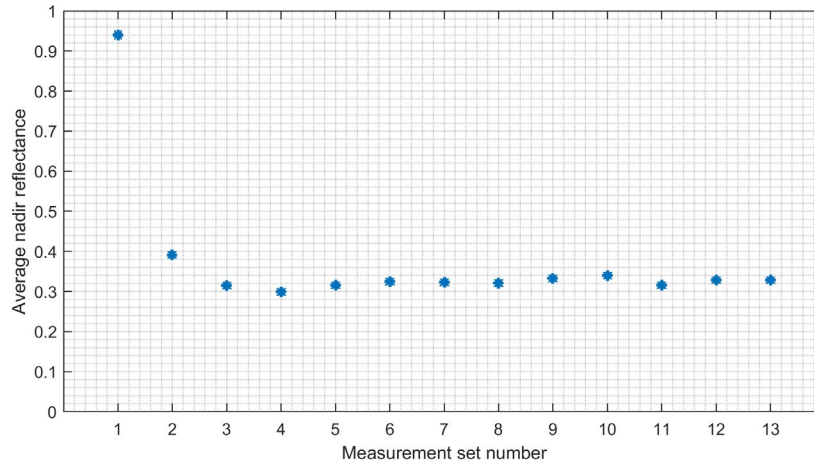


*Figure 7: Nadir reflectances measured during each of the 13 measurement sets, averaged over all wavelengths.*

All eight of the nadir HCRFs measured during the first measurement set were much higher than the typical reflectance measured at the playa, and one of the nadir HCRFs in the second set was similarly elevated. These issues are likely caused by an issue with the reference panel cross-calibration that was performed before each measurement set, as noted in the instrument operation notes for the first measurement set. Due to these issues, the first and second measurement sets were excluded from the correction factor calculation. This reduced the data matrix to a size of  $6 \times 36 \times 61 \times 11$ .

## 2.1 Band Averaging

The largest dimension of the data matrix was the wavelength, since the ULGS-II collected hyperspectral readings at each view configuration. The goal of this research was to calculate and apply BRF-based correction factors to GVR reflectance data corresponding to Sentinel-2A and -2B overpasses. An existing GVR data product supplied nadir surface reflectance data interpolated

to the time of a Sentinel-2 overpass and fitted to Sentinel-2 MSI bands. It was therefore convenient to fit the ULGS-II HCRF data to MSI bands as well.

Figure 8 shows the average nadir spectral surface reflectance measured by the ULGS-II during the measurement sets collected after 16:45 UTC on May 3<sup>rd</sup>, 2018. Also shown are the relative spectral responses (RSRs) of bands 1 through 9 of MSI on Sentinel-2 platforms A and B.

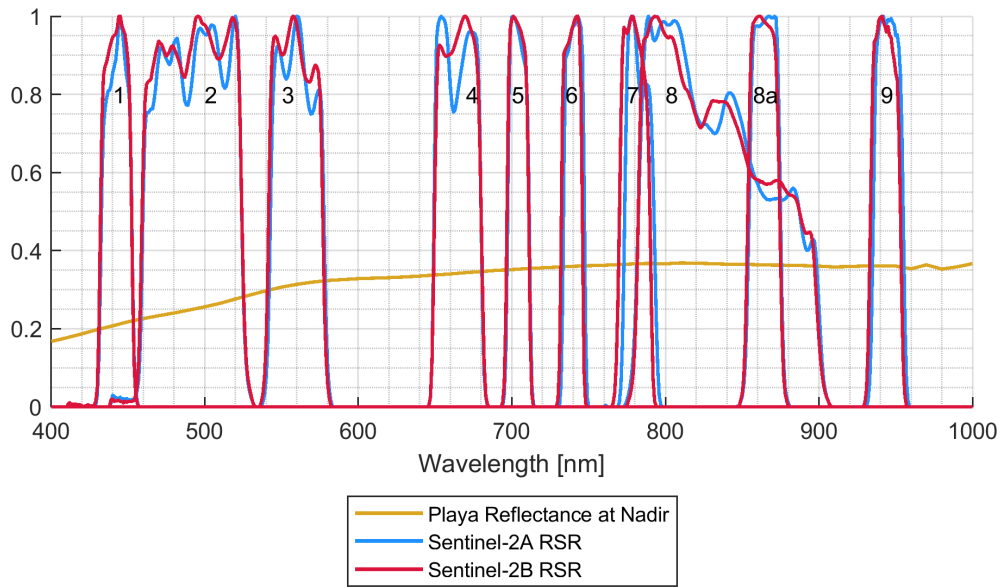


*Figure 8: Average spectral reflectance measured at nadir by ULGS-II on May 3<sup>rd</sup>, 2018 and relative spectral responses of MSI bands 1–9 on Sentinel-2A and -2B.*

First, the ULGS-II measurements were linearly interpolated to 1 nm intervals to match the MSI RSRs. Then, for every HCRF in each measurement set, the band average was taken for each of the 10 MSI bands on Sentinel-2A and -2B using the following equation:

$$HCRF(\theta_i, \phi_i, b, m) = \frac{\int_{\lambda_1}^{\lambda_2} HCRF(\theta_i, \phi_i, \lambda, m) RSR(\lambda, b) d\lambda}{\int_{\lambda_1}^{\lambda_2} RSR(\lambda, b) d\lambda}$$

Here,  $\theta_i$  and  $\phi_i$  are the view zenith angle and view azimuth angle at which the HCRF was measured,  $b$  refers to the MSI band, and  $m$  refers to the measurement set. After the band average of each HCRF was calculated, the data matrix was reduced to a size of  $6 \times 36 \times 20 \times 11$ .

## 2.2 Shadow Removal and Azimuth Conversion

As described in Section 1.1, the BRF of a surface is a function of four angles: the zenith and azimuth angles of the illuminating ray, and the zenith and azimuth angles of the viewer. For isotropic sites such as the playa, the view and illumination azimuths can be replaced by the relative azimuth, which is the angular difference between the illumination and view azimuths.

The ULGS-II records view azimuths relative to the instrument mast, but the instrument's orientation relative to north is not recorded. However, the solar azimuth during a measurement set can be determined by locating the shadow of the goniometer arm in the reflectance data. The affected data are then removed and the azimuths of the remaining measurements are converted to relative azimuths. The BRF for an isotropic site should be symmetric about the solar principal plane, so at this point the data is also averaged with a flipped copy of itself (such that HCRFs at relative azimuths of  $10^\circ$  are averaged with HCRFs at relative azimuths of  $350^\circ$  and so on) and only relative azimuths ranging from  $0^\circ$  to  $180^\circ$  need to be considered. This reduces the size of the data matrix to  $6 \times 18 \times 20 \times 13$ . Figure 9 shows the Sentinel-2A MSI band 5 HCRF values collected in the 5<sup>th</sup> measurement set before and after shadow removal and azimuth conversion.

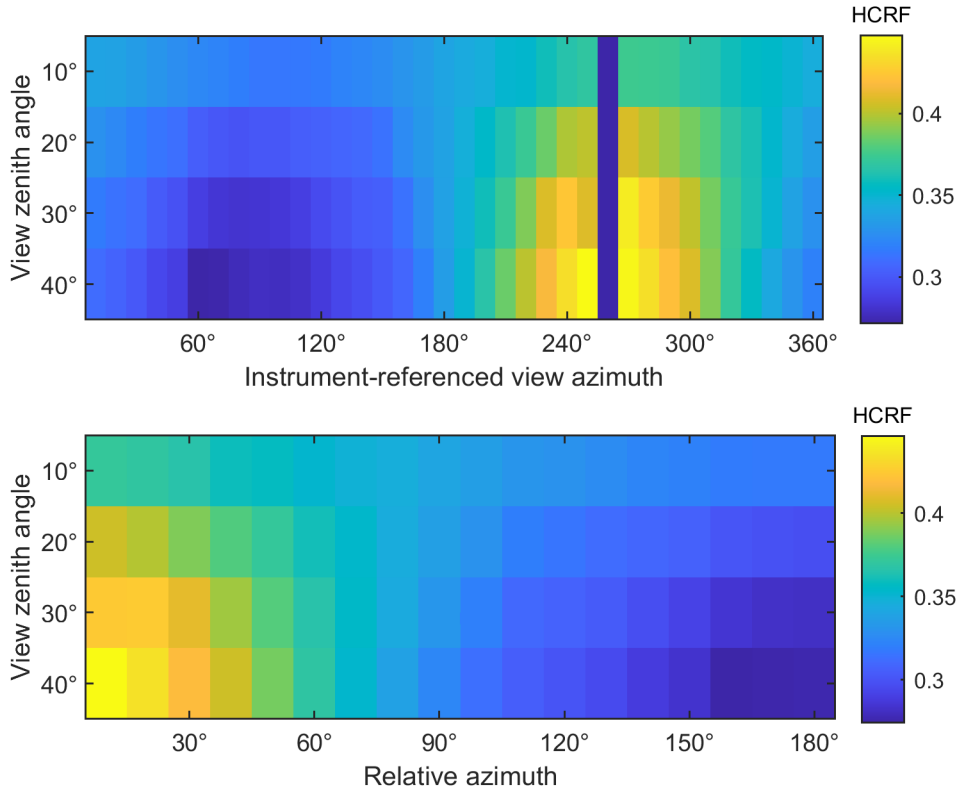


*Figure 9: HCRF data collected by ULGS-II at approximately 18:00 UTC on May 3<sup>rd</sup>, 2018 in Railroad Valley Playa. Results shown have been band-averaged to correspond to Sentinel-2A MSI band 5. The top plot features a shadow at 260° instrument-referenced azimuth angle indicating the solar azimuthal position. The data in the bottom plot have been shifted such that the azimuth angle refers to the angle to the solar principal plane and the shadow has been removed.*

### 2.3 Correction Factor Calculation

Once the data have been processed as described, the actual correction factor calculation is very simple. The correction factor is a function of view zenith angle, relative azimuth angle, spectral band, and measurement set, with the latter corresponding to the solar zenith angle. It is calculated as the HCRF at the desired band and view and illumination configuration normalized by the HCRF measured at nadir for the same band and measurement set.

$$CF(\theta_i, \phi_r, b, m) = \frac{HCRF(\theta_i, \phi_r, b, m)}{HCRF_{nadir}(b, m)}$$

This results in correction factors that are  $>1$  in the backscatter region, and  $<1$  in the forward scatter region, as shown in Figure 10.

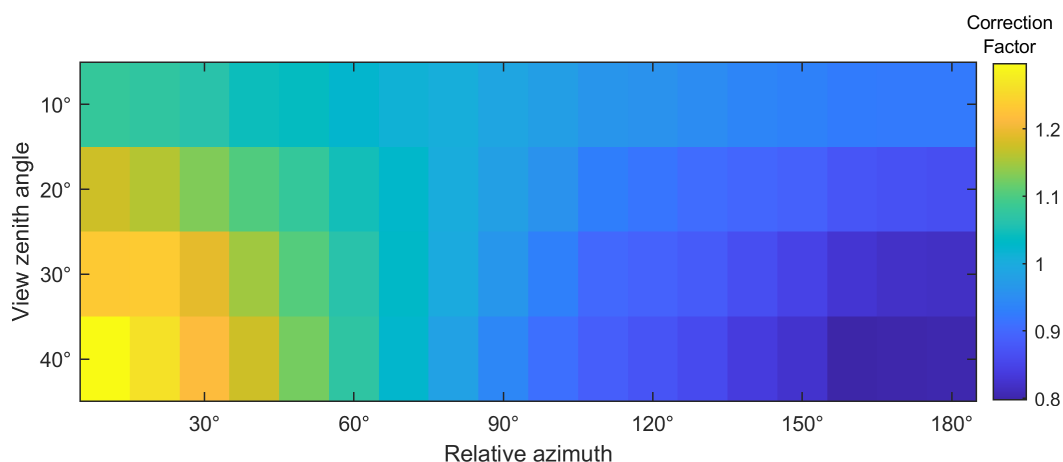
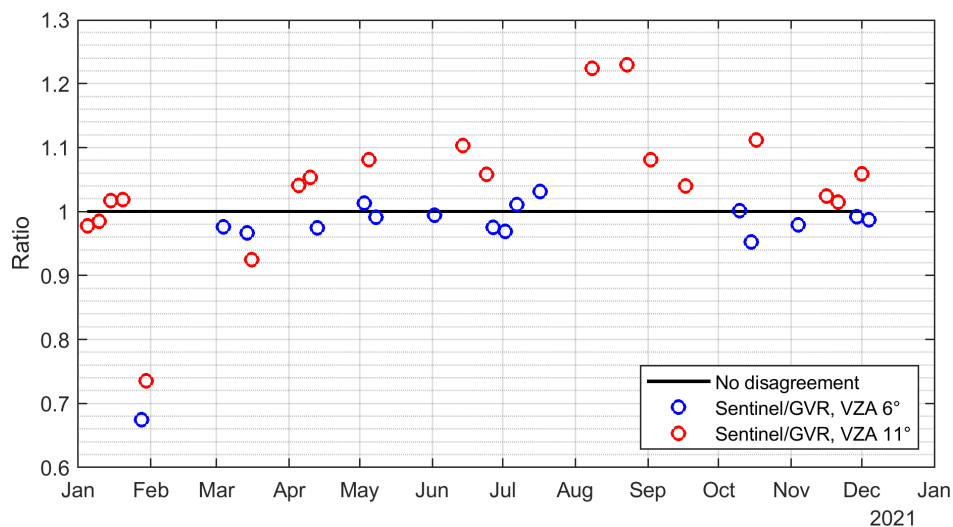


Figure 10: Correction factors determined using the HCRF data that are shown in Figure 9.

#### 2.4 Sentinel-2A and -2B MSI Data

Now that the correction factors have been calculated, they are ready to apply to real data. Sentinel-2A and -2B regularly pass over the playa in one of two view configurations. In one view configuration, they view RadCaTS at a zenith angle of about  $6.0^\circ$  and an azimuth angle of  $284.6^\circ$  (as measured from the ground site frame of reference), and in the other they view the site at a zenith of about  $11.2^\circ$  and an azimuth angle of  $103.0^\circ$ . Users of RadCalNet have reached out to the Remote Sensing Group in the past because MSI results from these two view angles often show a bias with both each other and with the GVR measured surface reflectances. There were 35 overpass days in 2021 which met the RadCalNet criteria for a ‘good’ day. Figure 11 shows the ratio of the Sentinel-2A and -2B MSI BOA surface reflectance values to the corresponding surface reflectances measured by the RadCaTS GVRs. All values have been averaged over MSI spectral bands 1–9.



*Figure 11: BOA surface reflectance values measured by GVRs and Sentinel-2 during 2021. Values have been averaged over all MSI bands of interest.*

Note that Sentinel results based on data collected from the  $6^\circ$  view zenith angle configuration tends to agree well with the GVR results, while the  $11^\circ$  view zenith angle tends to result in BOA surface reflectance values greater than the GVR results, especially during the summer months. Although the satellites view the playa at the same two absolute azimuth angles, the solar azimuth angle varies throughout the year, resulting in the varying relative azimuth angles shown in Figure 12.

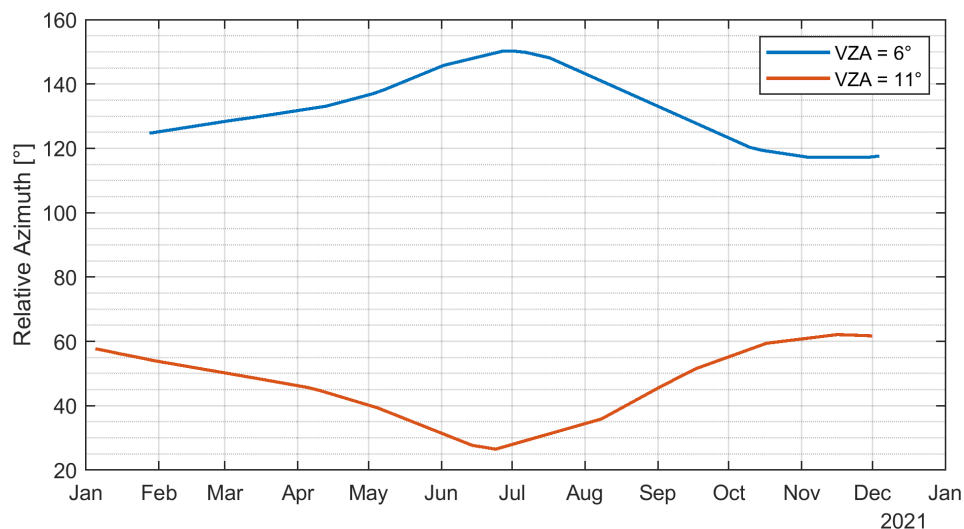


*Figure 12: Relative azimuth angle vs. time of year for each of the Sentinel-2 view configurations. A relative azimuth of  $0^\circ$  corresponds to the backscatter direction.*

In the correction factor results shown in Figure 10, values  $>1$  tended to occur close to the backscatter direction. This agrees with the data shown in Figures 11 and 12, as higher reflectances tend to be measured by the view configuration that approaches the backscatter direction.

## 2.5 Averaging Datasets

As explained in Section 1, the BRDF of a surface depends on the view configuration and the illumination configuration, both of which are described by a zenith angle and an azimuth angle. In the case of this data, the illumination zenith angle corresponds to the solar zenith angle, which is sampled by collecting HCRF data at multiple times of day. Unfortunately, the datasets collected by the ULGS-II span a more limited range of solar zenith angles than those that occur during the 2021 Sentinel-2 overpasses. This is illustrated in Figure 13.

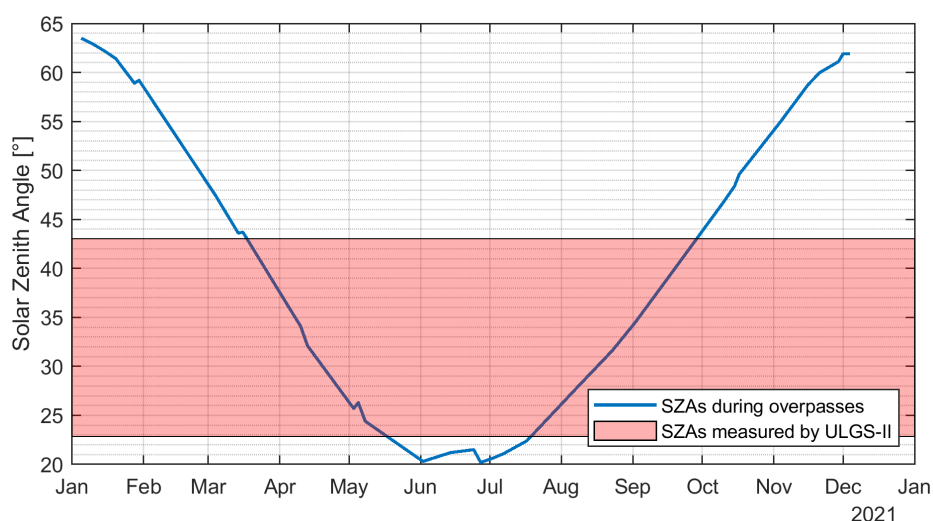


*Figure 13: Solar zenith angles during 2021 Sentinel-2 overpasses of Railroad Valley Playa. Red indicates the range of solar zenith angles sampled by the ULGS-II on May 3<sup>rd</sup>, 2018.*

As shown previously in Figure 7, the nadir reflectances were fairly constant for each of the 11 datasets used in the correction factor calculation. Analysis of HCRF measurements for other view angles showed similar invariance with solar zenith angle, particularly over the range of view zenith and relative azimuth angles spanned by the Sentinel-2 overpasses, which are indicated in Figure 14.

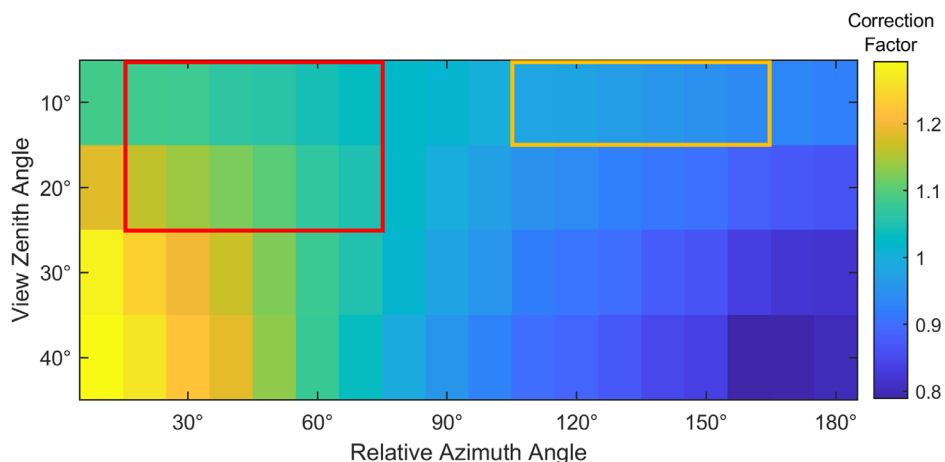


*Figure 14: Correction factors from Figure 10 with the range of Sentinel-2 overpass view angles indicated. Sampled HCRF angles for the 11° overpass configuration are indicated in red and angles for the 6° configuration are shown in yellow.*

The standard deviation of the data with respect to the dataset is shown in Figure 15 for MSI band 5 (704 nm). Other bands showed similar results.

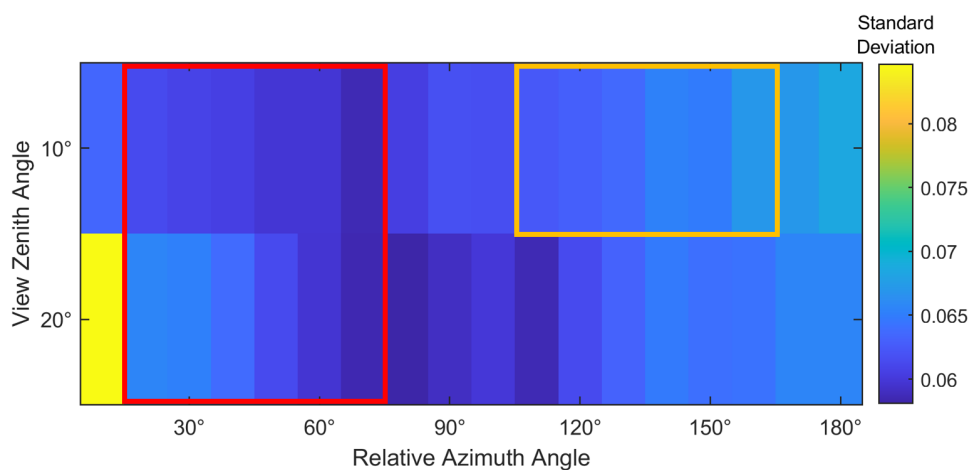


*Figure 15: Standard deviation of MSI band 5 correction factors with respect to dataset. Values corresponding to 11° and 6° overpass configurations are again indicated in red and yellow, respectively.*

The variation between correction factors for the same view and relative azimuth tends to be minimal, and the variation which does occur does not appear to be a function of solar zenith angle. For example, consider the correction factors for 20° view zenith, 20° relative azimuth. This view configuration has the greatest variability between datasets out of all the configurations in the

overpass angle range, but the variation does not appear to be correlated with the solar zenith angle, as illustrated in Figure 16.

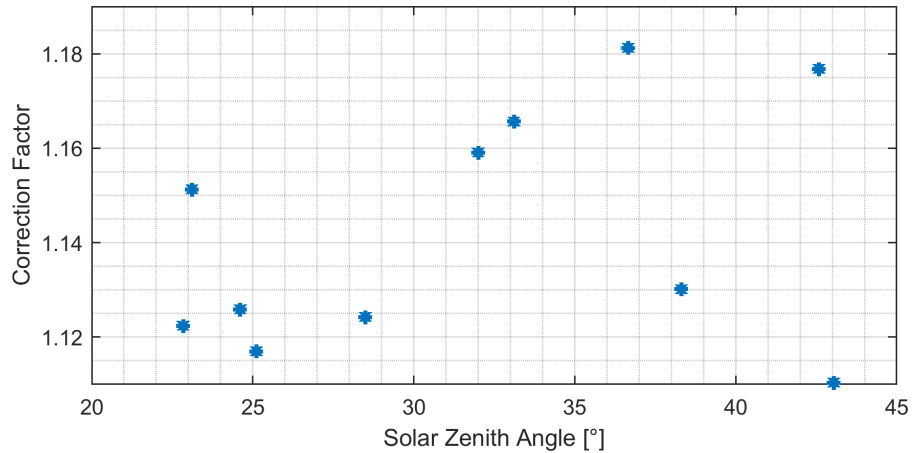


*Figure 16: Correction factors calculated from HCRF data for view zenith  $20^\circ$ , relative view azimuth  $20^\circ$ , and MSI band 5 plotted against the solar zenith angle during the HCRF measurement.*

Based on this trend, the correction factors are assumed to be invariant with solar zenith angle for the view angles studied. This allows the data to be averaged over all measurement sets, which reduces the size of the data matrix to  $6 \times 18 \times 20$  and allows the correction factors to be applied to all of the 2021 overpass data.

## Section 3 – Results

### 3.1 Application of Correction Factors

At this point, the data have been processed into a  $6 \times 18 \times 20$  matrix of correction factors, corresponding to 6 view zenith angles from  $10^\circ$  to  $60^\circ$ , 18 relative azimuth angles from  $10^\circ$  to  $180^\circ$ , and the total of 20 MSI bands between Sentinel-2A and -2B. For each of the 35 chosen overpasses in 2021, the correction factors were linearly interpolated to the satellite view zenith and relative azimuth. They were then used to scale the GVR-measured surface reflectance and calculate the expected BOA surface reflectance measured by the off-nadir-viewing MSI as follows:

$$R_{MSI,expected}(\theta_i, \phi_r, b) = CF(\theta_i, \phi_r, b)R_{GVR,nadir}(b)$$

The percent disagreement between the GVR and MSI reflectances were then calculated both with and without the BRF correction factor:

$$\% \text{ Error, uncorrected} = \frac{|R_{GVR,nadir} - R_{MSI}|}{R_{MSI}} \times 100$$

$$\% \text{ Error, corrected} = \frac{|R_{MSI,expected} - R_{MSI}|}{R_{MSI}} \times 100$$

The results for all 35 overpasses are shown in Figure 17.

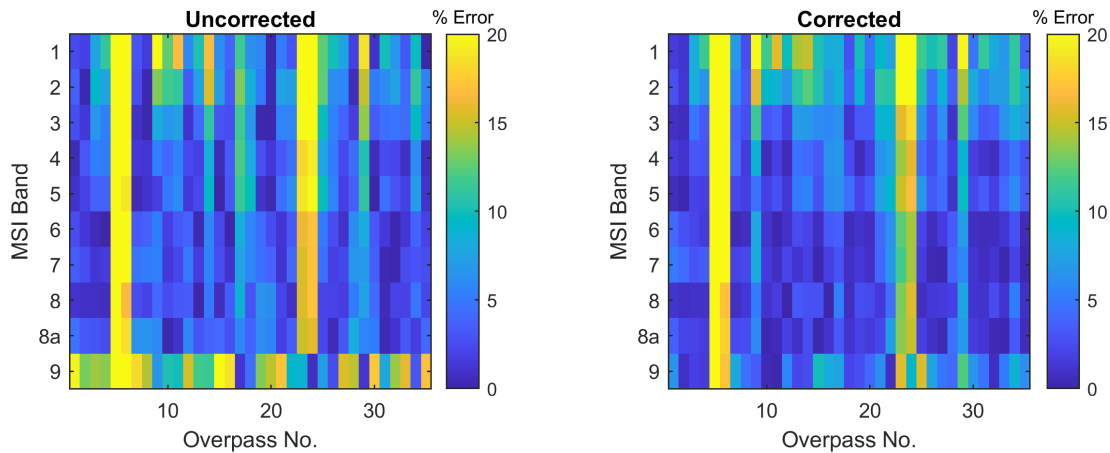


*Figure 17: Percent error between uncorrected (left) and corrected (right) GVR-measured reflectances and MSI-derived BOA surface reflectances.*

The improvements in agreement due to the correction factor are most visible in MSI bands 6 through 9. Additional trends are visible when the results are separated depending on the viewing geometry of the overpass. Figure 18 shows the results for overpasses with an  $11^\circ$  view zenith angle.

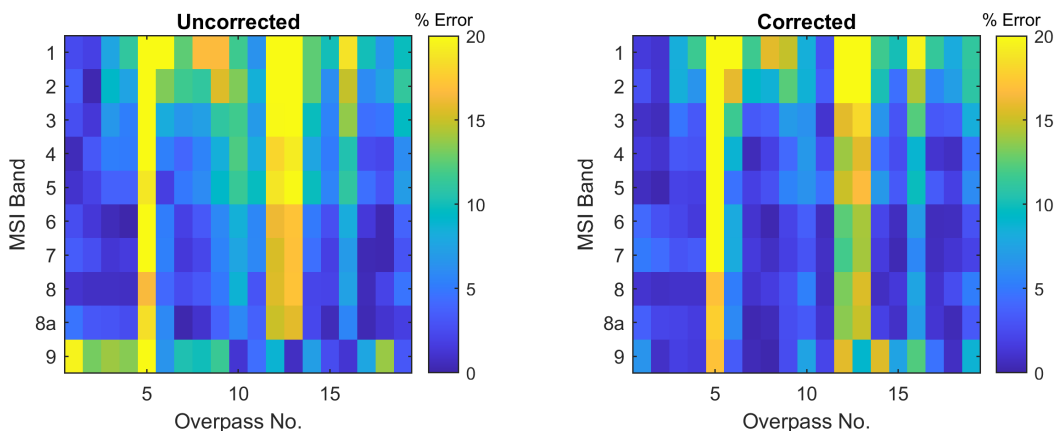


Figure 18: Percent error for  $11^\circ$  VZA overpasses before and after correction.

Neglecting the three high-error overpasses for the moment, consider the plot on the left of Figure 18. The error tends to be higher for overpasses between 5 and 15, corresponding to the middle of the year. That is also when the  $11^\circ$  VZA overpasses have relative azimuths closest to the backscatter direction, which in turn correspond to higher BRFs. In the plot on the right, those mid-year errors are mostly reduced by the application of the correction factor.

The  $6^\circ$  overpass data (shown in Figure 19) shows slight improvement for bands 6–8a, and significant improvement for band 9. However, disagreement between GVR and MSI reflectances for bands 1–5 appears to increase after the correction factor is applied.

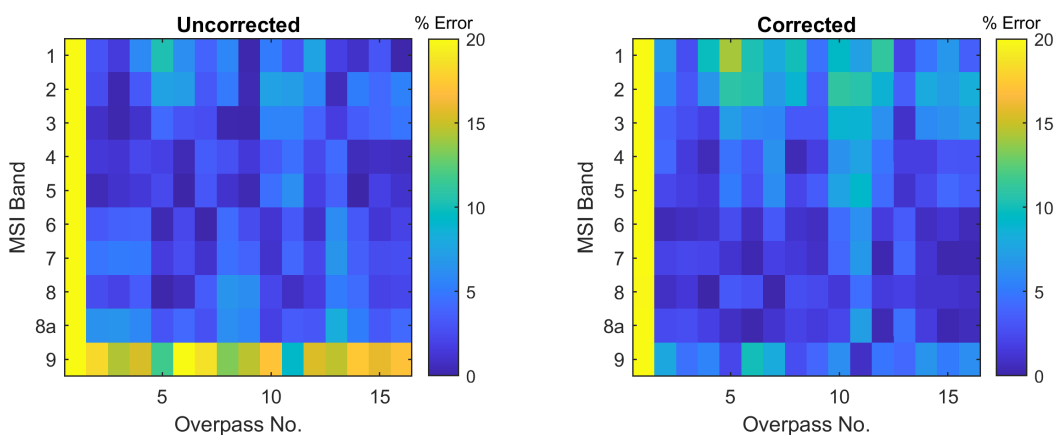


Figure 19: Comparisons using uncorrected and corrected GVR reflectances for  $6^\circ$  overpass.

There are multiple overpasses within this time period for which the error appears to be  $>15\%$  for all bands. These mostly correspond to days on which the GVR-measured surface reflectance was lower than normal, possibly due to wet surface conditions. The GVR surface reflectances for all

2021 overpasses are shown in Figure 20, averaged over all MSI bands. The average surface reflectance is also shown, and one standard deviation below the average is indicated with a dashed line.

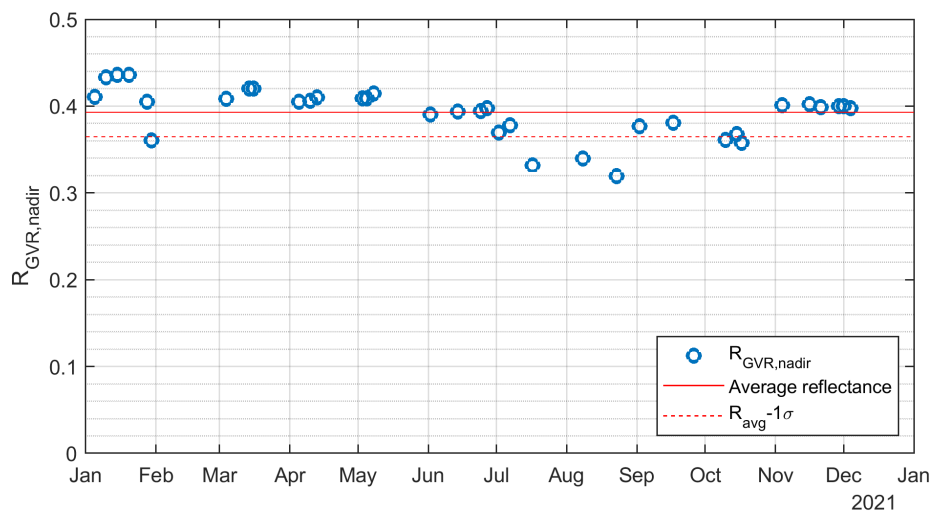


Figure 20: Average surface reflectance vs. time for 2021 Sentinel-2A and -2B overpasses.

The ULGS-II HCRF measurements were collected in May of 2018, when the surface was dry. It is possible that the BRF properties of the playa are different when the surface is wet. Figure 21 shows the percent difference between GVR and MSI BOA reflectance for both the  $11^\circ$  VZA and  $6^\circ$  VZA overpasses.

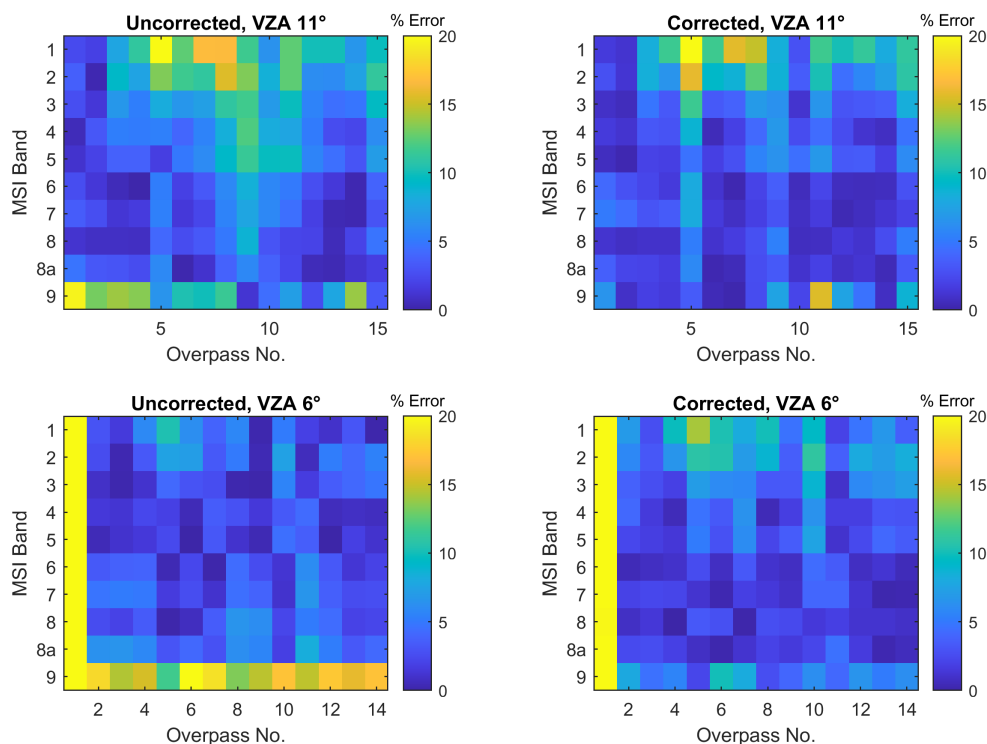


Figure 21: Percent error plots with low reflectance dates removed.

Removing the low reflectance dates removes most of the overpasses with high disagreement for all bands. The improved agreement for the 11° VZA overpasses is now more apparent, with the mid-year overpasses seeing the greatest improvement. The results for the 6° overpass are less promising. While the uncorrected 6° VZA overpasses tend to have better agreement between GVR and MSI reflectances, the application of correction factors does not consistently improve agreement. MSI bands 6 through 9 agree better with BRF-corrected GVR results, but bands 1 through 5 seem to get worse. It is possible that at low view zenith angles, BRF effects are small compared to other errors.

### 3.2 Sources of Uncertainty

This thesis explores the application of BRF correction factors calculated from a very limited model of the RadCaTS surface properties. As such, there are several sources of uncertainty. First and foremost, the ULGS-II HCRF data represents an extremely limited model of the playa BRDF. The correction factors were calculated from data that were collected once, on one day, in one location within the test site. The degree to which the BRF of the specific site measured matches that of the

rest of the test site cannot be inferred from this data, nor can the temporal variability of the BRF properties.

The ULGS-II instrument itself also contributes to the uncertainty of the results. The instrument records view azimuth angles relative to the instrument mast. As described in Section 2.2, the solar azimuth angle can then be found by locating the shadow of the goniometer arm in the raw HCRF data. However, the instrument only sampled the azimuthal angles in  $10^\circ$  increments, leading to uncertainty in the relative azimuth angles of the measurements. The arm might also partially shade adjacent azimuths, adding uncertainty to the HCRF measurements collected within  $10^\circ$  of the shadow.

Another source of error in determining the relative azimuth angle is the change in the solar azimuth angle during a measurement set. During the measurement set collected closest to solar noon, the sun moved more than  $7^\circ$  azimuthally. This is not corrected for when calculating correction factors for specific overpasses.

Another issue present in the ULGS-II data is reflection anomalies. In each of the datasets there are hotspots in roughly the forward scatter direction. These hotspots appear for view zenith angles of  $60^\circ$  when the sun is high, and drift towards view zenith angles of  $40^\circ$  to  $50^\circ$  when the sun is low, suggesting that the effect is due to sunlight directly entering the spectroradiometer foreoptic rather than reflecting off of some specular component of the playa surface.

## Section 4 – Conclusion

The surface reflectance properties of Railroad Valley Playa are significantly non-Lambertian. This causes errors when measurements by nadir-viewing GVRs are compared to BOA surface reflectance products of wide-FOV spaceborne sensors, such as MSI on Sentinel-2A and -2B. Preliminary results using correction factors derived from HCRF measurements show promising improvements for several overpasses, especially when the satellite measurements were collected from a view configuration near the backscatter direction. However, a more robust model of the playa BRF is needed before BRF-based correction factors can be added to the RadCaTS RadCalNet site for use with wide FOV sensors.

## References

- [1] K. J. Thome, S. F. Biggar, and W. Wisniewski, "Cross comparison of EO-1 sensors and other Earth resources sensors to Landsat-7 ETM+ using Railroad Valley Playa," *IEEE Transactions on Geoscience and Remote Sensing*, 41 (6), 1180–1188 (2003).
- [2] H. H. Kieffer, and R. L. Wildey, "Establishing the Moon as a Spectral Radiance Standard," *Journal of Atmospheric and Oceanic Technology*, 13 (2), 360–375 (1996).
- [3] P. N. Slater, S. F. Biggar, J. M. Palmer, and K. J. Thome, "Unified approach to absolute radiometric calibration in the solar-reflective range," *Remote Sensing of Environment*, 77 (3), 293–303 (2001).
- [4] K. J. Thome, "Absolute radiometric calibration of Landsat 7 ETM+ using the reflectance-based method," *Remote Sensing Environment*, 78 27–38 (2001).
- [5] K. P. Scott, K. J. Thome, M. R. Brownlee, "Evaluation of Railroad Valley Playa for use in vicarious calibration," *Proc. SPIE 2818, Multispectral Imaging for Terrestrial Applications*, (4 November 1996).
- [6] J. Czapla-Myers, "Atmospheric measurement analysis for the Radiometric Calibration Test Site (RadCaTS)," *Proc. SPIE 9607, Earth Observing Systems XX*, 96070A (8 September 2015).
- [7] J. S. Czapla-Myers, K. J. Thome, B. R. Cocilovo, J. T. McCorkel, J. H. Buchanan, "Temporal, spectral, and spatial study of the automated vicarious calibration test site at Railroad Valley, Nevada," *Proc. SPIE 7081, Earth Observing Systems XIII*, 70810I (20 August 2008).
- [8] N. Anderson, J. Czapla-Myers, N. Leisso, S. Biggar, C. Burkhart, R. Kingston, and K. Thome, "Design and calibration of field deployable ground-viewing radiometers," *Appl. Opt.*, 52 (2), 231–240 (2013).
- [9] N. J. Anderson, and J. S. Czapla-Myers, "Ground viewing radiometer characterization, implementation and calibration applications: a summary after two years of field deployment," in *Proc. SPIE, 88660N–88660N-10* (2013).
- [10] B. N. Holben, T. F. Eck, I. Slutsker, D. Tanré, J. P. Buis, A. Setzer, E. Vermote, J. A. Reagan, Y. J. Kaufman, T. Nakajima, F. Lavenue, I. Janjowiak, and A. Smirnov, "AERONET - A Federated Instrument Network and Data Archive for Aerosol Characterization," *Remote Sensing Environment*, 66 1–16 (1998).
- [11] A. Berk, G. P. Anderson, P. K. Acharya, L. S. Bernstein, L. Muratov, J. Lee, M. Fox, S. M. Adler-Golden, J. J. H. Chetwynd, M. L. Hoke, R. B. Lockwood, J. A. Gardner, T. W. Cooley, C. C. Borel, P. E. Lewis, and E. P. Shettle, "MODTRAN5: 2006 update," in *Proc. SPIE, 62331F–62331F-8* (2006).

- [12] J. Hankerson, "Automated Motion Control of a Ground-Viewing Radiometer System" (Unpublished master's thesis). University of Arizona (2018).
- [13] K. J. Thome and P. Nandy, "Accuracy of ground-reflectance calibration of imaging spectroradiometers at large sensor view angles", Proc. SPIE, Vol. 4132, pp. 260 - 268, 2000.
- [14] G. Schaepman-Strub, M.E. Schaepman, T.H. Painter, S. Dangel, J.V. Martonchik, "Reflectance quantities in optical remote sensing—definitions and case studies, Remote Sensing of Environment," Volume 103, Issue 1, 2006, Pages 27-42, ISSN 0034-4257.
- [15] N. Leisso, and J. Czapla-Myers, "Comparison of diffuse sky irradiance calculation methods and effect on surface reflectance retrieval from an automated radiometric calibration test site," in Proc. SPIE, 815310 –11 (2011).
- [16] P. Nandy, K. Thome, and S. Biggar, "Characterization and field use of a CCD camera system for retrieval of bidirectional reflectance distribution function," *J. Geophys. Res.*, 106(D11), 11957– 11966, (2001) doi:10.1029/2000JD900390.
- [17] C. J. Bruegge, M. C. Helmlinger, J. E. Conel, B. J. Gaitley, and W. A. Abdou, "PARABOLA III: A sphere-scanning radiometer for field determination of surface anisotropic reflectance functions", Remote Sens. Rev., in press, 2000.
- [18] W. Abdou, M. Helmlinger, J. Conel, C. Bruegge, S. Pilorz, J. Martonchik, and B. Gaitley, "Ground measurements of surface BRF and HDRF using PARABOLA III," Journal of Geophysical Research. 106. 11967-11976 (2001) 10.1029/2000JD900654.
- [19] C. J. Bruegge, C. Coburn, A. Elmes, M. C. Helmlinger, F. Kataoka, M. Kuester, . . . , F. M. Schwandner (2019). Bi-directional reflectance factor determination of the railroad valley playa. *Remote Sensing*, 11(22), 2601. doi:http://dx.doi.org/10.3390/rs11222601
- [20] C. A. Coburn, and S. D. Noble, "ULGS II: A High-Performance Field and Laboratory Spectrogoniometer for Measuring Hyperspectral Bidirectional Reflectance Characteristics," IEEE Transactions on Geoscience and Remote Sensing, 54(4), 2304-2313 (2016).